SAND2021-7687C

Tracking Turbulent Spots on a Hypersonic Cone at Angle of Attack using Temperature-Sensitive Paint

Anshuman Pandey*, Katya M. Casper†, John T. Flood‡, Rajkumar Bhakta § Russell Spillers ¶ Steven J. Beresh‖
Sandia National Laboratories, Albuquerque, NM 87185

This study explores the evolution of a turbulent spot in a hypersonic boundary layer over a sharp cone at an angle attack. The spot has been periodically generated using an electric-discharge excitation of the boundary layer and its thermal footprint has been captured using temperature-sensitive paint (TSP). The presence of the spot has been verified using schlieren visualization and surface-mounted pressure and temperature sensors. Spot trajectories at several different angles of attack have been extracted using the TSP data and compared with streamlines obtained using numerical simulations for an undisturbed boundary layer. The results indicate that for all angles of attack tested, the turbulent spot tracks more closely with edge streamlines than surface streamlines. At larger angles of attack, the spreading rate of the spot was found to be smaller and the spot trajectory diverged towards the wind side of the edge streamline.

I. Introduction

HYPERSONIC boundary layer transition refers to the phenomenon when the boundary layer developing over a hypersonic vehicle changes from a laminar state to a turbulent state. It is associated with a dramatic increase in surface pressure fluctuations, heating and skin friction [1] which can affect not only the performance but also the integrity and safety of the vehicle. The state of the boundary layer also strongly affects the shock-wave/boundary layer interaction phenomenon associated with flow deflections induced by the vehicle geometry. While studies have used canonical geometries to further the understanding of transition phyics at zero angles of attack, there is limited knowledge base on the routes to boundary layer turbulence for a pitched geometry. To this end, the current experimental work was carried out to characterize boundary layer transition on a canonical sharp nose cone at an angle of attack.

In a low-disturbance environment, transition of a boundary layer typically occurs through the following steps [4]: receptivity mechanisms govern the acoustic, entropic or vortical disturbances in the free-stream that enter the boundary layer and excite the instabilities; these primary instabilities undergo modal growth until a point where the mean flow

*Postdoctoral Appointee, Engineering Sciences Center, Member AIAA
†Principal Member of the Technical Staff, Engineering Sciences Center, Senior Member AIAA
‡Graduate Intern, Engineering Sciences Center, Member AIAA
§Senior Test Operations Engineer, Engineering Sciences Center
¶Principal Technologist, Engineering Sciences Center
‖Distinguished Member of the Technical Staff, Engineering Sciences Center, Associate Fellow AIAA

itself becomes affected; the deformed mean flow becomes susceptible to secondary instabilities that have much higher growth rates and cause swift transition to turbulence. The breakdown of instability wave-packets result in intermittent generation of turbulent spots. Further downstream, the spots merge into a fully turbulent boundary layer. In contrast, in a high-disturbance environment or when a large disturbance is locally introduced, the first few steps are expedited or even bypassed and a turbulent spot is promptly generated [5]. The turbulent spots are essentially localized patches of turbulence i.e. the vortical structures, transport processes and boundary layer statistics within turbulent spots are similar to that in a fully-developed turbulent boundary layer [6–8]. The passage frequency of these spots at a given downstream location governs the intermittency [9] of the boundary layer which is the fraction of time it can be characterized as laminar or turbulent. This intermittency factor can be used for linear combination of the laminar and turbulent boundary layer parameters to obtain estimates of the time-averaged boundary layer parameters during transition [10]. The high pressure and heating fluctuations during transition are directly related to the passage of the turbulent spots which switch the pressure and heating loads between the laminar and turbulent states. It is thus important to characterize and understand the dynamics of turbulent spots.

Experimental studies focusing on the evolution of turbulent spots have typically employed artificial introduction of localized disturbance such as using a spark perturber [11] to obtain reliable and periodic turbulent spots which can be analyzed using ensemble-averaging techniques. These studies have revealed the arrow-head structure of the turbulent spots [12, 13] which grows in a cone of influence and this growth has been shown to be self-similar [14]. Under small pressure gradients, the growth and spreading rates are similar [15] but have been reported to be slower under stronger favorable pressure gradients [16] and at higher Mach numbers [17, 18]. In the hypersonic regime, turbulent spots have been experimentally studied on the tunnel nozzle walls [19, 20], shock-tube walls [21] and on flat plates [22], blunted cylinders [23] and cones [24, 25] in hypersonic tunnels. The use of high-frequency surface pressure [19], temperature [22–24] and optical [20, 21] measurements in these experiments have provided detailed information about the spot structure, convection speeds and spreading/growth rates.

The aforementioned studies have been confined to spots with nominally straight trajectory i.e. on straight tunnel walls or on cones at zero angle of attack. However, the evolution of a turbulent spot on a hypersonic cone at an angle of attack has not been explored. A pitched cone experiences a pressure gradient from a maximum at the windward ray to a minimum at the leeward ray. This pressure gradient induces a crossflow component to the boundary layer streamlines which becomes stronger with increasing angle of attack. This crossflow component produces an inflection point and the resulting instability, known as the crossflow instability, generates vortices that transfer momentum between the freestream and the boundary layer. The downwash regions of these vortices produce stagnation heating that show up as heat streaks in the experiments. The secondary instabilities that arise due to the mean flow distortion induced by these vortices are understood as the primary route to turbulence on a pitched cone. However, there is limited understanding on the transitional aspects of the flow especially the behavior of the turbulent spots that are a precursor to turbulence.

Specifically, there exists a few key open questions regarding the development of the turbulent spots in the boundary layer of a pitched cone: 1. What trajectory do the turbulent spots follow? 2. What is the spreading rate? 3. What is the effect of angle of attack on this behavior? To this end, experiments have been conducted in the Sandia Hypersonic Wind Tunnel on a 7° half angle sharp cone at Mach 8. The thermal footprint of the turbulent spots generated through an electric discharge in the boundary layer have been tracked using temperature-sensitive paint (TSP) and supplementary measurements have been made using surface pressure and temperature sensors and schlieren. The following section describes these experimental techniques and the results are presented in the subsequent section.

II. Experimental Setup

A. Sandia Hypersonic Wind Tunnel and Test Conditions

The Sandia Hypersonic Wind Tunnel (HWT) is a conventional blowdown-to-vacuum facility. The tunnel employs an interchangeable system of nozzles and heater sections which enable Mach number in the test section to be set at 5, 8 or 14. In this work, the experiments were only conducted Mach 8. HWT-8 uses 689 MPa Nitrogen supplied from a bottle farm. It has a P_0 range of 1720–6890 kPa, T_0 range of 500–890 K, which provides a Reynolds number (Re) range from 3.3–20 $\times 10^6$/m. Noise levels vary from 3–5% [25]. A pitching-arc mechanism in conjunction with extension tubes allow variations in the angle of attack (α) and the streamwise location (with respect to the test section) of the wind-tunnel model. The arc, powered by a hydraulic motor, can be initiated with a preset move-and-hold trajectory to allow measurements at multiple angles of attack during a run. All testing was carried out in the low Re range of 3.8–6.4 $\times 10^6$/m to ensure that the turbulent spots are studied in an otherwise laminar boundary layer.

B. Model: Sensors and Perturber

The test model is a 7° half-angle slender cone with a base diameter of 0.127 m. Fig. 1 shows a schematic of the stainless-steel model tested in this work. The cone comprises four conic sections which combine to form the overall assembly: the first section is 76.2 mm long and has a sharp nose tip (radius less than 50 μm) and is followed by the 101.6 mm long perturber frustum that has an insert to house the perturber electrodes. The following two frustums that are 235.9 mm and 103.4 mm long, comprise the bulk of the cone and have several axial and circumferential inserts with appropriate holes for sensor placement. In this work, high-frequency surface pressure sensors: Mic-062 Kulites with A-screens and PCB-132s have been used to capture the fluctuations induced by the spot passage in an axial and a circumferential insert. The locations are described in Table 1 and are represented in Fig. 1. Labels of KA and PA correspond to the Kulites and the PCBs on the axial insert and the same holds for the KC and PC labels which are on the circumferential insert. MSBA corresponds to the Medtherm Schmidt-Boelter gauge on the axial insert and MTCA and MTCW are the Medtherm thermocouples on the axial insert and windward side insert respectively. Data from only a few sensors in this list has been discussed in this work and analysis of other sensors will be presented in a future work.

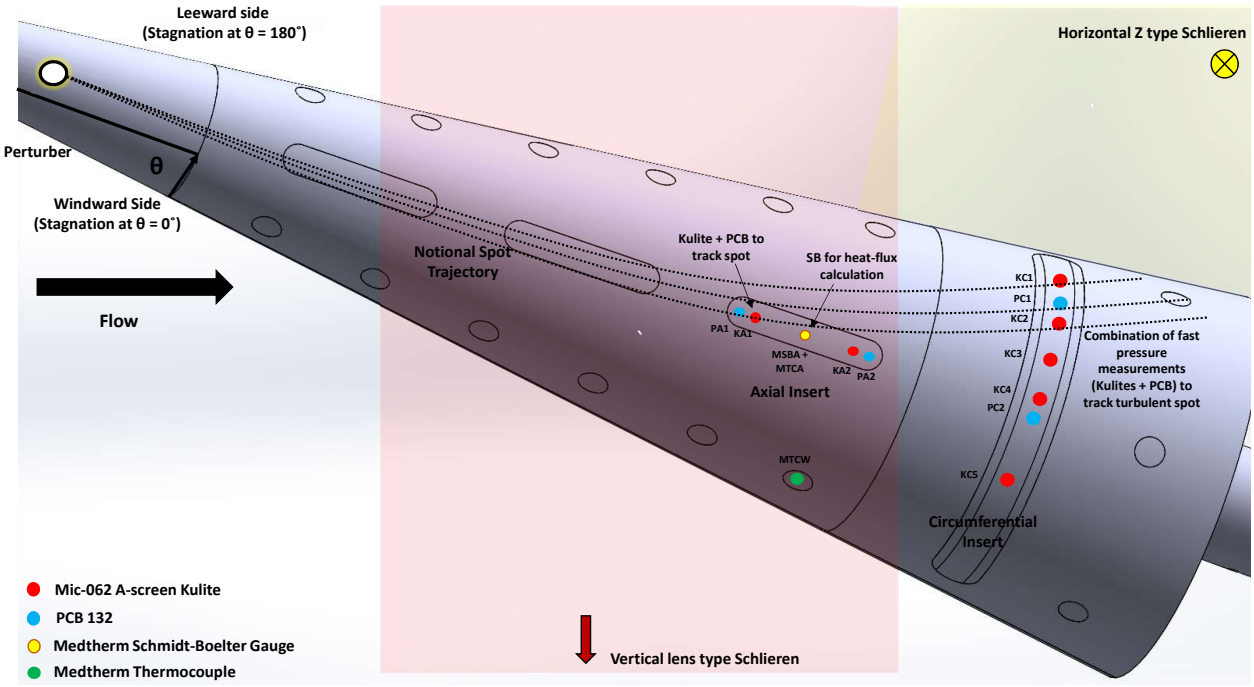

Fig. 1 Schematic of the model and instrumentation layout. Sensors are not to scale

The coordinate system is centered about the nose with the x axis pointing downstream along the axis of the cone and θ representing the angle that a ray pointing downstream from the nose along the cone surface makes with the windward ray i.e. the windward and leeward rays corresponds to $\theta = 0°$ and $\theta = 180°$ respectively. Measurements were made at $\alpha = 0° - 6°$.

The disturbances for generating the periodic spots were introduced into the cone boundary layer using an electrical discharge perturber housed in the second frustum section. Electrical sparks were generated by supplying a voltage of 2 kV across the perturber electrodes. Customized electronics allow variable pulse widths with repetition rates up to 10 kHz. For a given run condition, appropriate pulse widths were selected to obtain a reliable spark which was visualized using a video camera. Repetition rate of 8-10 kHz was used in most cases to generate a continuous stream of spots that would leave a thermal footprint strong enough to be captured using TSP. The two electrodes of the perturber, spaced 6.35 mm apart, were aligned axially and were centered at x = 0.137 m. Independent rotation of the frustums with respect to the cone enable placement of the perturber and the sensors at any ray angle. This allows a sweep of the turbulent spot generation location in the non-axisymmetric flowfield generated by a cone at an angle of attack. For the work discussed in this paper, the perturber and the axial insert were kept in line i.e. at the same ray angle. Results are presented for perturber locations of $\theta = 70°$ and $\theta = 80°$. The sampling rates for the PCB, Kulite and thermocouples were 2.5 MHz, 500 kHz and 95 Hz respectively. The Kulite and PCB signals were low-pass filtered at 200 kHz and 1 MHz respectively. A high voltage probe that measured the voltage generated by the electric-discharge perturber was sampled at the same

rate as the PCBs to aid in the temporal correlation between the signals.

Table 1 Instrumentation location on the model

Instrumentation Label	Description	x (m)	Ray angle with respect to the axial insert (°)
Perturber	Electrical discharge perturber to induce spots	0.137	0
PA1	1st PCB on the axial insert	0.208	0
KA1	1st Kulite on the axial insert	0.218	0
MSBA + MTCA	Medtherm Schmidt-Boelter gauge and thermocouple	0.229	0
KA2	2nd Kulite on the axial insert	0.239	0
PA2	2nd PCB on the axial insert	0.249	0
KC1	1st Kulite on the circumferential insert	0.452	52.5
PC1	1st PCB on the circumferential insert	0.452	45.0
KC2	2nd Kulite on the circumferential insert	0.452	37.5
KC3	3rd Kulite on the circumferential insert	0.452	22.5
KC4	4th Kulite on the circumferential insert	0.452	7.5
PC2	2nd PCB on the circumferential insert	0.452	0
KC5	5th Kulite on the circumferential insert	0.452	-22.5
MTCW	Medtherm thermocouple on the wind-side	0.394	-60

C. High-Speed Schlieren

For tracking the turbulent spots, high-speed schlieren visualization was conducted in the two axes allowed by the four windows of the HWT. Only the results from the vertical schlieren setup have been discussed here. This setup used a pair of 101.6 mm diameter spherical lenses for light collimation and 152.4 mm diameter plane mirrors for folding the collimated beam through the top and bottom windows of HWT-8. The schlieren visualized the port side (the same side as the perturber) boundary layer and was movable to capture a length of about 100 mm (limited by the collimated beam diameter) along the cone surface. Typically, the central part of the cone was visualized using the vertical schlieren as shown in Fig. 1. A high-speed laser (Cavilux Smart - 648 nm wavelength) with a pulse width of 1 ns was used as the light source and the density gradients were captured using a high-speed camera (Phantom v2512). The cameras were mounted on tilt stages such that the sensor axis could be aligned with the cone surface. Typical frame rates were 190 kHz with an array size of 1280x96 and the resolution was about 11.5 pixels/mm.

D. Temperature-Sensitive Paint

The model was painted with temperature-sensitive paint (TSP) to visualize the boundary-layer transition and separation regions on the model. The TSP formulation used was Ru(bpy) in a clearcoat [27]. The paint was excited with 460-nm water-cooled lights (ISSI) and images were acquired with 16-bit cameras (LaVision Imager sCMOS) at 20 Hz. A picture of the experimental setup is shown in Fig. 2. A 615 nm band-pass filter with 26 nm full width-half maximum was used to capture only the paint emission and eliminate contamination from the laser used for simultaneous schlieren

visualization. The image intensities were converted to temperature using the paint calibration. During a run, the TSP images were acquired for 20 seconds with the perturber starting halfway (at 10 seconds) during the acquisition. This provided the heating pattern on the cone with and without the perturber. Typically, two TSP cameras were used to view the cone from the top and the port side windows of the HWT. These cameras were stereo calibrated to enable triangulation of the TSP images that was then mapped onto a cone grid. The mapping between the cone coordinates and the TSP images allowed extraction of the spot trajectory as well as superposition of the computational streamlines on the experimental images.

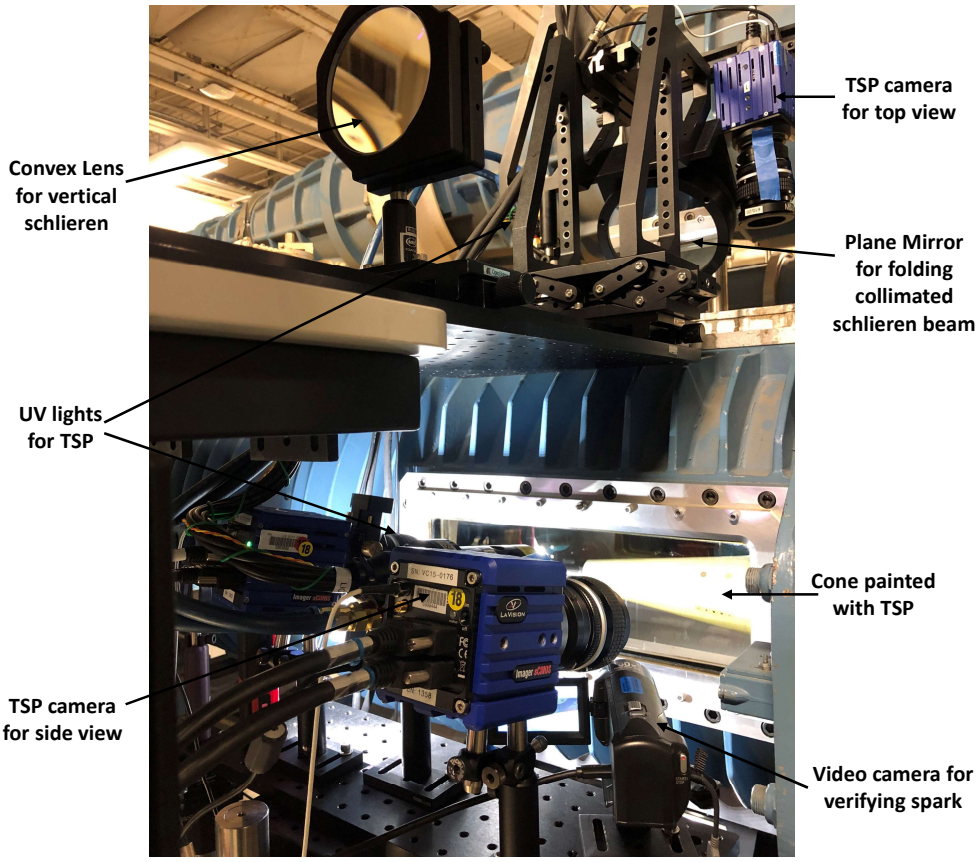

Fig. 2 Picture of the experimental setup showing instrumentation on the west-side and top window

E. Computational streamlines

Computational fluid dynamic simulations of the cone at angle of attack were conducted using US3D. These were used to extract the edge and surface streamlines on the cone at angle of attack and also provided the mean surface pressures on the inclined cone. The computational grid extended through x = 400 mm for $\alpha = 0°, 1°, 2°, 4°$ and through the end of the cone (x = 517 mm) for $\alpha = 6°$. All simulations were carried out for Re = 6.0 x 10^6/m. Fig. 3 shows the surface streamlines on the cone for the $\alpha = 4°$ case.

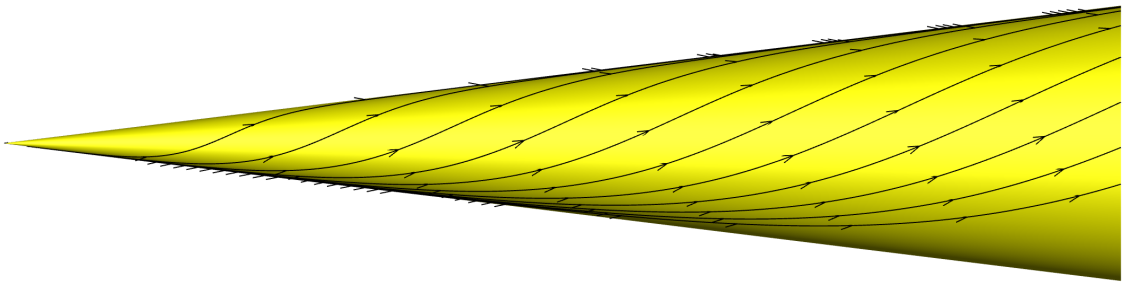

Fig. 3 Computational surface streamlines on a cone at α = 4°

III. Results

A. Effect of the generated disturbance

In this study, electric discharge excitation has been used to induce boundary layer disturbances that develop into turbulent spots and evolve along the cone. This section shows some measurements confirming the successful creation of disturbances that are then tracked in the next section using TSP. First, a series of instantaneous schlieren images are shown in Fig. 4 for $\alpha = 2°$ at Re = 6.4 x 10^6/m. The images show the passage of a nascent turbulent spot marked using white arrows. The characteristic rope-like wave-packets of the Mack 2nd mode instability are also visible in the approximately 2 mm thick boundary layer. The growing turbulent spot is markedly thicker and more diffuse than the otherwise laminar boundary layer and is distinctly visible in the schlieren images. A couple of probes, marked in the bottom panel in Fig. 4, have been used in this schlieren field of view for comparing the spectral contents of the features within and outside the boundary layer. Power spectral density (PSD) of the intensity fluctuations at those points are shown in Fig. 5. The probe in the boundary layer shows spectral peaks at 10 kHz and 20 kHz which correspond to the spot generation frequency and its higher harmonic whereas outside the boundary layer, only broadband free-stream noise is picked up by the schlieren. These results indicate that turbulent spots are being generated at the desired frequency.

Fig. 6 compares timeseries of the PCB data for an $\alpha = 0°$ run at Re = 5.2 x 10^6/m. The forcing frequency was 8 kHz. The PCB signals in the figure have been normalized and shifted in the y direction for clarity. The perturber firing instants, located every 0.125 milliseconds, are shown using the black dotted lines. PA1, PA2 and PC2 are in line with the perturber (see Fig. 1 and Table 1) and the generated disturbances travel over these sensors for $\alpha = 0°$. At high Mach numbers such as that tested here, the 2nd Mack mode is the dominant instability mode in the boundary layer and multiple wave-packets can be seen across all signals especially at PA1 where the forced disturbance strength is still weak. Further downstream as the disturbance grows, the intermittency of the boundary layer increases thereby decreasing the prevalence of the 2nd mode wavepackets. In contrast to a wavepacket that has several symmetric signal undulations at a well-defined frequency, a turbulent spot pressure signature is much more chaotic and consists of sharp spikes and asymmetric fluctuations. Passage of three cycles of generated spots over the sensors are marked in the PC1 signals in Fig. 6 using black arrows.

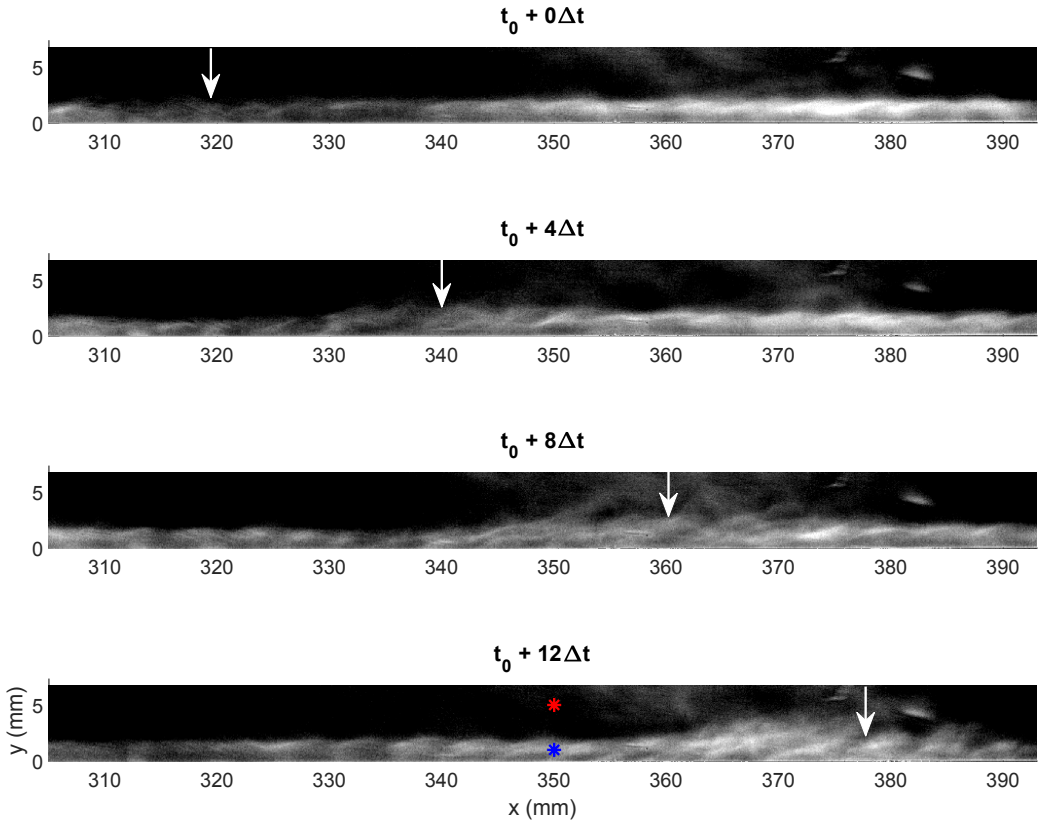

Fig. 4 Instantaneous schlieren images for $\alpha = 2°$, Re = 6.4 x 10^6/m. Every 4th image is shown where Δt is the time delay between the images of the sequence; arrows in each panel mark the turbulent spot location. Red and blue dots in the bottom figure show the locations used for calculation of PSD in Fig. 5

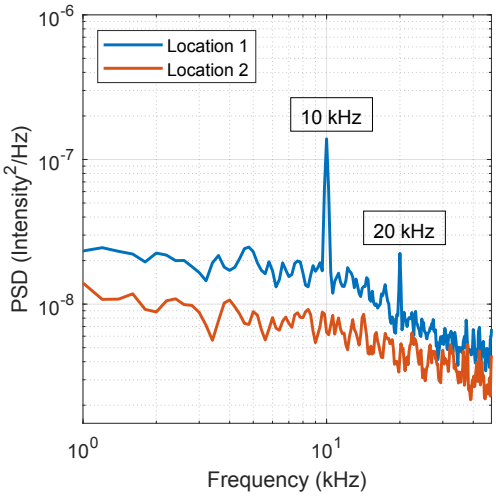

Fig. 5 PSD for intensities at the locations shown in Fig. 4. $\alpha = 2°$, Re = 6.4 x 10^6/m

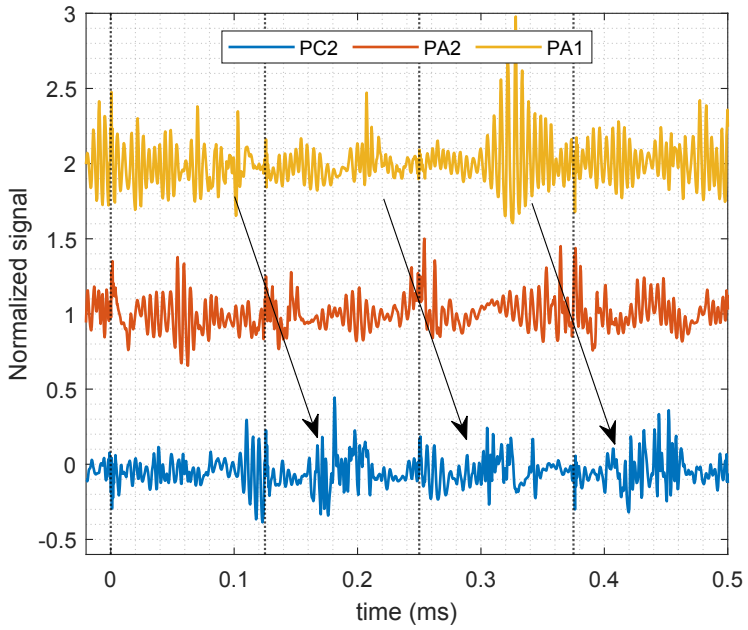

Fig. 6 Time series of signals for $\alpha = 0°$, Re = 5.2 x 10^6/m. PA1 and PA2 have been shifted up for clarity. Black dotted lines indicate the perturber firing instants. Black arrows indicate the disturbance signatures.

The above behavior can also be observed in the frequency space as shown in Fig. 7 for the $\alpha = 4°$, Re = 6.4 x 10^6/m. Since the cone is pitched, the streamlines and the spot trajectory curve away from PC2 and instead go over PC1 in this case (see trajectory in Fig. 14). A comparison of the PC1 data before and after the perturber switches on shows that the continuous stream of introduced disturbances decrease the boundary layer content at the 2nd mode frequency of 190 kHz. Along with a decrease in the 2nd mode energy and its harmonic, the energy in the higher frequencies increase after the perturber turns on. This suggests an increase in the turbulent content in the boundary layer as also seen in the time series data in Fig. 6 along with a corresponding decrease in time with the the 2nd mode instability content.

Fig. 8 shows the thermocouple data for the $\alpha = 0°$ run discussed above. Data acquisition was started 0.5 seconds before the perturber was initiated. Both the sensors report a monotonic increase in model temperature due to aerodynamic heating by the freestream during the course of the experiment. MSBA, which is on the axial insert in line with the perturber (see Fig. 2 and Table 1), shows a noticeable rise in temperature at 0.5 seconds as the perturber starts firing and a sharp drop after another 10 seconds when it stops. This observation is in agreement with the increased thermal footprint of an intermittent boundary layer due to the periodic passage of the forced turbulent spots. In the next section, this increase in temperature has been used to track the trajectory of the disturbances using TSP.

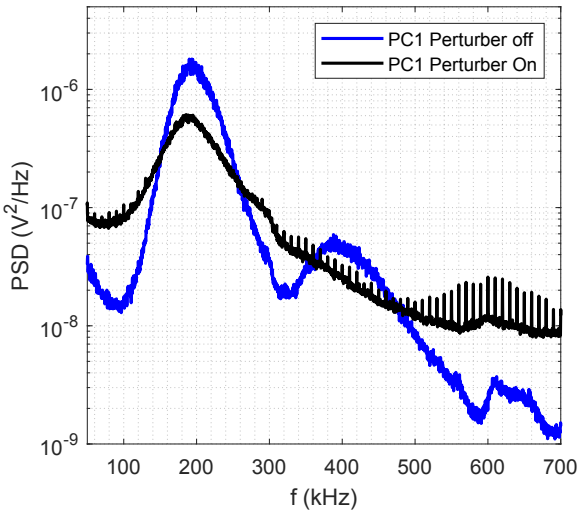

Fig. 7 Comparison of PSD of PC1 signal before and after the perturber turns on. α = 4°, Re = 6.4 x 10^6/m. Spot trajectory shown in Fig. 14(a)

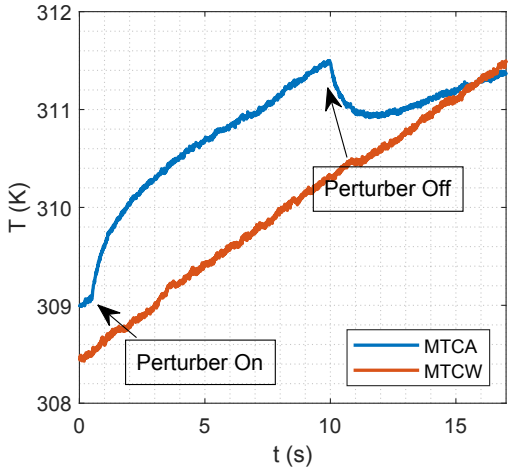

Fig. 8 Comparison of thermocouple data on (MSBA) and offset (MSBW) from the perturber ray. α = 0°, Re = 5.2 x 10^6/m

B. Spot trajectory tracking using TSP

1. Extraction of trajectory

The data presented in the previous section demonstrated that the turbulent spots introduced by the perturber are significant to induce density, pressure and heating fluctuations in the boundary layer. In contrast to the point based thermocouples, TSP provides full field temperature measurements that enable tracking of the disturbance on the cone surface. Fig. 9 shows the temperature contours (colorbars not shown for brevity) for an α = 1.9° run at Re = 6.4 x 10^6/m with θ = 70°. The images have been averaged over a 20 image segment and then smoothed using 3x3 pixels median and box filter. Both the undisturbed and the perturbed cases shows increased heating on the lee side and the wind side of the

cone. The wind side heating is due to the stagnation of the freestream and the lee side heating is related to the transition of the separated flow and the downwash induced by the streamwise vortices. During paint application, the amount of luminophore on the sensor inserts was not controlled which resulted in the inserts being brighter than the rest of the cone; as such the higher apparent heating on these inserts is not real. There is also an increased heating across the circumference of the base of the cone.

The overall temperatures in the perturber-on case (Fig. 9(b)) are higher as these images were taken after the perturber-off data. Also present in the perturber on data is a diffuse heating streak on the lee side of the axial insert that is the footprint of the turbulent spot. To enhance this heating streak, a square of the ratio of the perturber on to off cases was computed as shown in Fig. 9(c). The ratioing supresses the heating due to the phenomena common in both the cases and emphasizes the heating induced by the spot. This image was subsequently used for extraction of the spot trajectory. Near the base of the cone, the ratio incorrectly suggests a decrease in the heating due to the spot. However, it is expected that the spot continues to grow and cause increased heating but the ratio decreases due to the high temperature values present there in the perturber off images. The aforementioned sources of error in the TSP fields, i.e. the insert heating and the base circumference heating, have been found to affect the determination of the spanwise extent and the spreading rates of the spots. However, since the trajectory is determined by interpolation of the maximum heating location in the central region of the spot streak, it is expected to be less affected by these error sources.

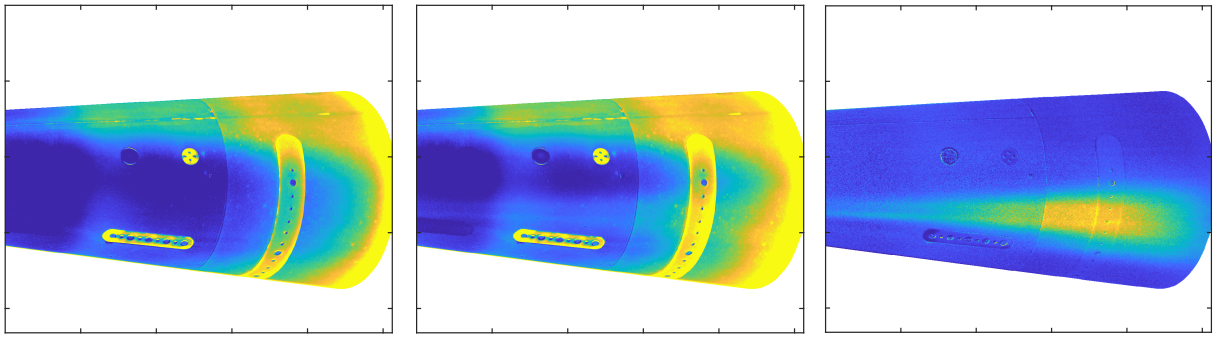

(a) (b) (c)

Fig. 9 α = 1.9°, Re = 6.4 x 10^6/m, θ = 70° (a) TSP images with perturber off; (b) TSP images with perturber on; (c) Square of the ratio of perturber on to perturber off images

To extract the spot trajectories, the ratioed image was mapped onto the x-θ coordinates for the cone. This image is shown in Fig. 10. First, at every x location, a smoothing spline (for large α) or a lorentz curve (for small α) was fitted to the ratioed data. This process is shown in Fig. 11 for a section taken at x = 420 mm in the TSP field shown in Fig. 10. A double derivative of this fitted curve was then computed and its peaks, representing a sharp change in the slope of the intensity, were identified as the spanwise edges of the spot. The upper (lee side) and lower (wind side) edges of the spot at this x location are identified in Fig. 11. In between these edges, the maximum location of the fitted curve was used

as the centerpoint of the spot. A 2nd degree polynomial was then fit to each set of points (lee side edges, wind side edges and the centerpoints) to obtain the trajectories shown in Fig. 10. The parabolic equation provided the necessary curvature to capture the downward (-ve θ) movement of the spot edges seen at low angles of attack; an example of this can be seen in the lower (lee side) edge of the spot in Fig. 10. This polynomial was forced to pass through the perturber location at x = 137 mm and θ = 70°; a slope was not prescribed at this location. Also shown in the figure are surface and edge streamlines obtained from numerical simulations for α = 2.0° and Re = 6.0 x 10^6/m that pass through the perturber location. Using the x-θ to image pixel mapping, both the extracted trajectory data and the computational streamlines could be mapped back to the original TSP image.

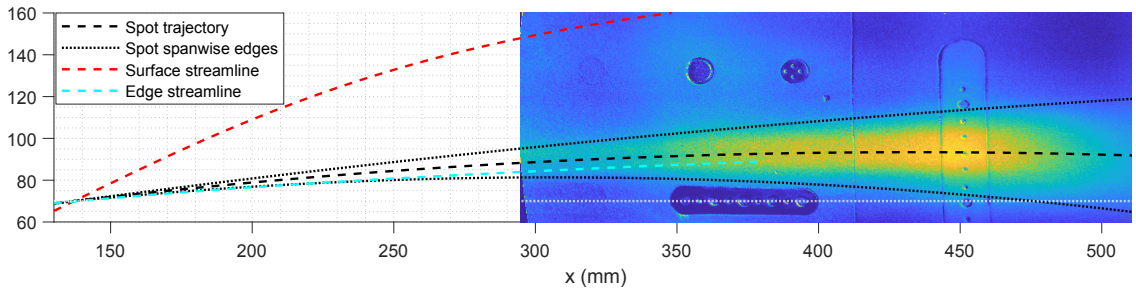

Fig. 10 Ratioed image mapped onto x-θ with curve fits to the spot trajectory. α = 1.9°, Re = 6.4 x 10^6/m, θ = 70°. Streamlines from simulations for α = 2.0°, Re = 6.4 x 10^6/m is also shown for comparison

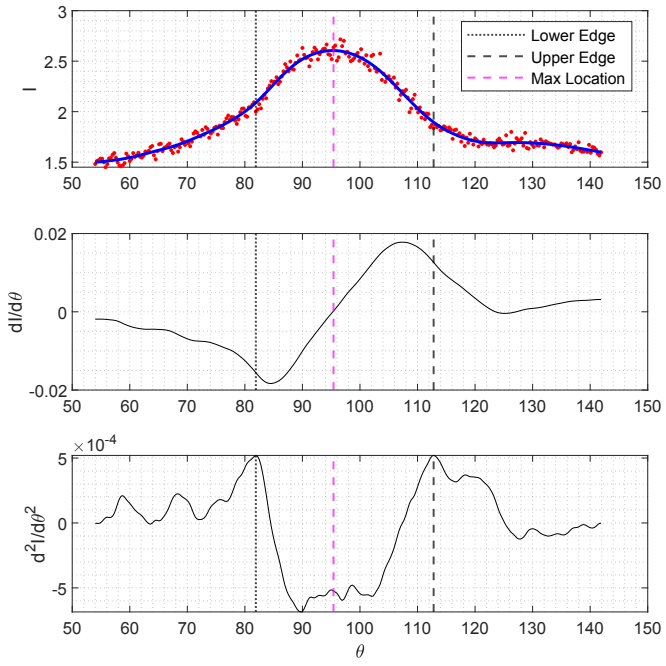

Fig. 11 Calculation of spot edges and centerline at x = 420 mm for the case discussed in Fig. 10. Top: Raw intensity values and its curve fit, Middle: Derivative of the curve fit, Bottom: Double derivative of the curve fit.

2. Small angles of attack

For a straight cone at a zero angle of attack, the streamlines follow the cone rays (constant θ) originating at the nose. A turbulent spot generated by introducing a disturbance at a given θ location on the cone would follow these streamlines while spreading in the spanwise direction as the spot grows [19, 25]. Fig. 12 shows the TSP heating measurements on the cone for such a case; a strong color scaling is used to emphasize the spot dimensions. The perturber was located at $\theta = 80°$ and the black dashed line that tracks the peak heating location is closely aligned to that. For this $\alpha = 0°$ case since the streamlines do not curve, a line fit instead of the 2nd degree polynomial was used. The dotted lines represents this fit to the spanwise edges of the spot which were found using a lorentz fit to the spot heating at each x location. These lines were constrained to be of the same slope in either direction of the centerline. A spreading angle of 4.7° provided the best fit with a 'virtual' spot initiation location of x = 300 mm. For an edge Mach number of 6.7 used in this experiment, this spreading angle is about 50% larger than the approximately 3.0° value suggested by the correlation provided by Fischer [17].

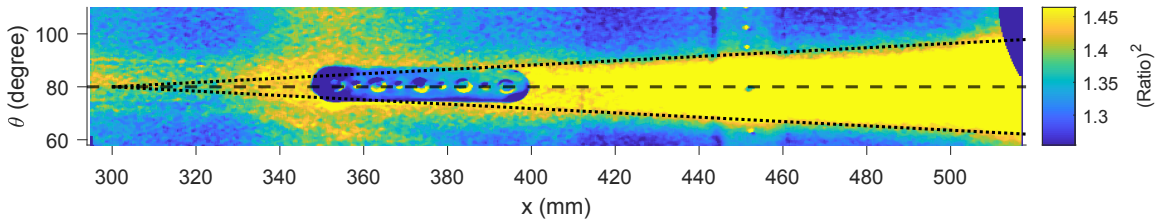

Fig. 12 x-θ TSP ratioed image. α = 0°, Re = 4.8 x 10^6/m, θ = 80°. Black dashed line shows streamline trajectory passing through the perturber and dotted lines are the lines fitted to the spanwise edges of the spot

Fig. 13 shows the square of the temperature ratios for the $\alpha = 1.0°$ and $\alpha = 1.9°$ cases. Superimposed on the figures are the tracked trajectories of the spot heating and the streamlines obtained from simulations. There is a close correspondence between the edge streamlines and the heating trajectory indicating that at low angles of attack, the disturbances generated by the perturber follow the edge streamlines. As discussed in the next section, a pair of heating streaks due to vortices generated by the perturber traverse along the lee side of the edge streamline. Upstream of the axial insert, the spot is expected to be less developed (see Fig. 12) and the surface heating is predominantly associated with these vortices. However as the turbulent spot develops and spreads in the spanwise direction, it engulfs these vortices. The diffuse heating in the two cases in Fig. 13 suggests that these vortices have also transitioned thus aiding in the development of the desired turbulent spot. The numerical streamlines are only available until x = 400 mm, but a visual comparison suggests that further downstream, the spot trajectory diverges to the wind side of the edge streamline. Spreading rate that depends on the curve fit to the spot edges appears to increase rapidly towards the base of the cone; however since the spot heating data is unavailable in this region, this spreading rate could be overexaggerated.

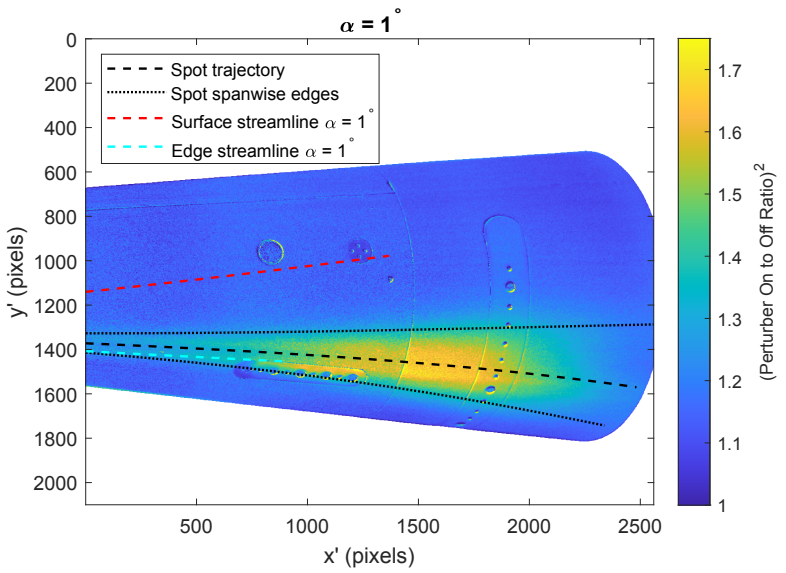

(a)

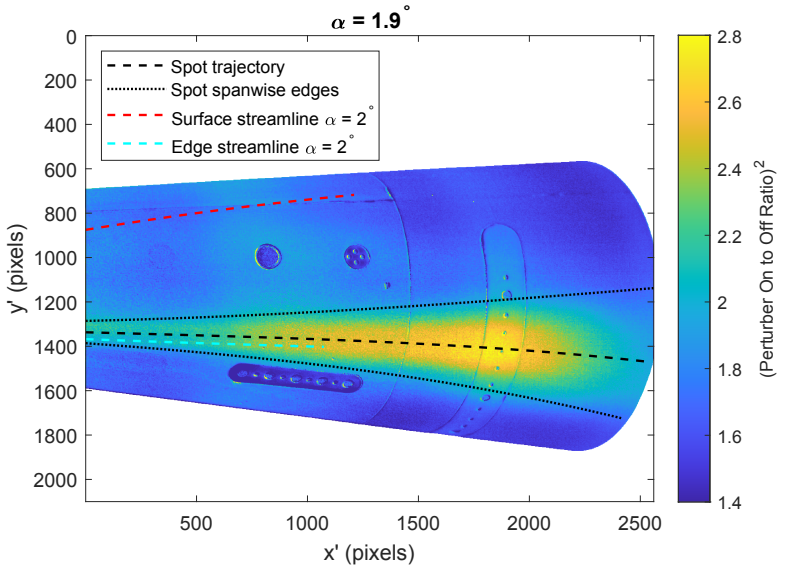

(b)

Fig. 13 Spot trajectories at small angles of attack θ = 70°, Re = 6.4 x 10^6/m (a) α = 1.0°; (b) α = 1.9°. Streamlines were computed at Re = 6.0 x 10^6/m

3. Large angles of attack

Fig. 14 shows the square of the temperature ratios for the α = 4.5° and α = 5.5° cases. The stronger pressure gradients at larger angles of attack generate larger crossflow that sweeps the surface streamlines close to the lee ray (θ = 180°). In the heating pattern of the disturbance, a pair of well-defined coherent heat streaks are visible in addition to a growing region of diffuse heating due to the developing turbulent spot. The origin of the heat streaks is not clear at this time but it could be a result of the flow blockage, during the duration of the pulse width, generated by the electric

discharge of the perturber. Such a blockage in the boundary layer would be associated with streamwise vortices that would transfer freestream momentum to the wall and generate the heat streaks. The frequency response of TSP is of the order of a few Hz, as such the TSP fields provide an integrated view of the heating over multiple cycles of perturber firing. Since the crossflow component is strong at larger angles of attack, the streamlines diverge rapidly and might be the reason why the streaks are clearly visible in Fig. 14 but were not in Fig. 13. A second explanation for the source of the observed streaks could be streamwise vortices generated as a result of a slight protrusion of the perturber electrodes into the boundary layer. Though no roughness was visually observed, a slight protrusion could result in generation of counter-rotating vortices that could cause the heating streaks as discussed above. In either case, since the heating streaks are clearly visible in the ratioed images, addition of the disturbance by the electric discharge perturber increases the intensity of these blockage or roughness induced vortices.

In order to track only the turbulent portion of the induced disturbance, the trajectory of the diffuse region was extracted in the x-θ coordinate using a spline fit to the heating pattern at each x location. The region of the coherent heat streaks was excluded from this analysis because as seen in Fig. 14 these streaks do not become turbulent until the end of the cone. An interesting result is that the spot trajectory (black dashed line) is on the wind side of the edge streamline (cyan dashed line). This could be related to the favorable azimuthal pressure gradient that diminishes the growth of turbulence on the lee side of the streamline and promotes growth on the wind side. This would cause the trajectory of a growing turbulent spot to diverge to the wind side of the edge streamline.

4. Trajectory and spreading rate of the spot

To summarize the findings in the previous subsections, Fig. 15 compares the trajectory for the different angles of attack with the edge streamlines passing through the perturber location. These trajectories were obtained using a 2nd order polynomial fit to the TSP data available only from x > 300 mm (marked using a dashed line) and as such the behavior of these curves in the upstream region may not be physical. For the zero degree case, the streamlines stay along the same θ while accelerating with a small favorable pressure gradient. In support of previous studies [25], the spot trajectory was found to align with this streamline. For small angles of attack, the spot centerline was observed to be on the lee side of the edge streamline but then, judging by the slope of the curves, it curved to the wind side; however, this could not be confirmed since edge streamline data was not available in the downstream part of the cone for these cases. As mentioned earlier, the heating upstream of the axial insert (x = 350 mm) for small α could be attributed to the heating streaks that do not diverge as in the large $alpha$ cases. This streak heating contributes to the extracted spot trajectory to be on the lee side of the edge streamline. For large α, the spot trajectory was predominantly on the wind side of the edge streamlines while the heat streaks straddled the lee side of these streamlines.

The edge streamline passing through the perturber location navigate a three-dimensional pressure field setup by the flow around the pitched cone. This asymmetric pressure field causes the flow streamlines to diverge from that of a

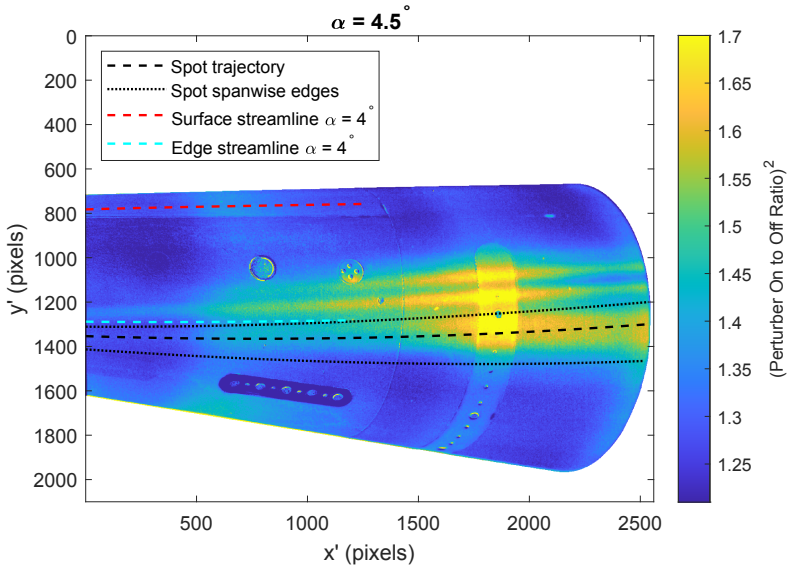

(a)

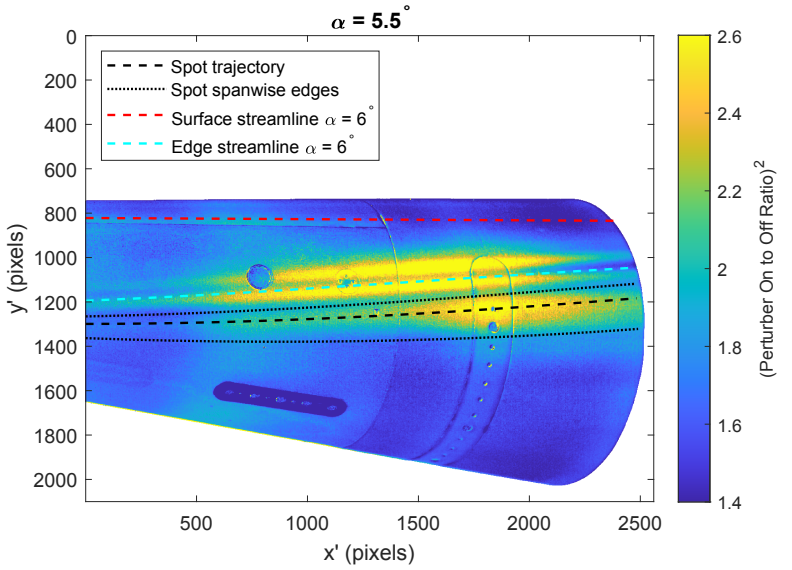

(b)

Fig. 14 Spot trajectories at large angles of attack θ = 70°, Re = 6.4 x 10^6/m (a) α = 4.5°; (b) α = 5.5°. Streamlines were computed at Re = 6.0 x 10^6/m

straight cone case. There exists pressure gradients along the streamlines that would affect the development of turbulence. Fig. 16(a) shows the mean pressure values and its gradients along the edge streamlines passing through the pertuber location at θ = 70° and x = 137 mm. Stagnation pressures on the wind side increase sharply with angle of attack. Since the pertuber efficiency improves with mean pressure and density, the increased pressure for the larger α cases might explain the strong blockage induced vortices observed in Fig. 14. As the streamline curves arouund the cone, the pressure values decrease sharply that results in strong -ve streamwise pressure gradients. These values are shown in Fig.

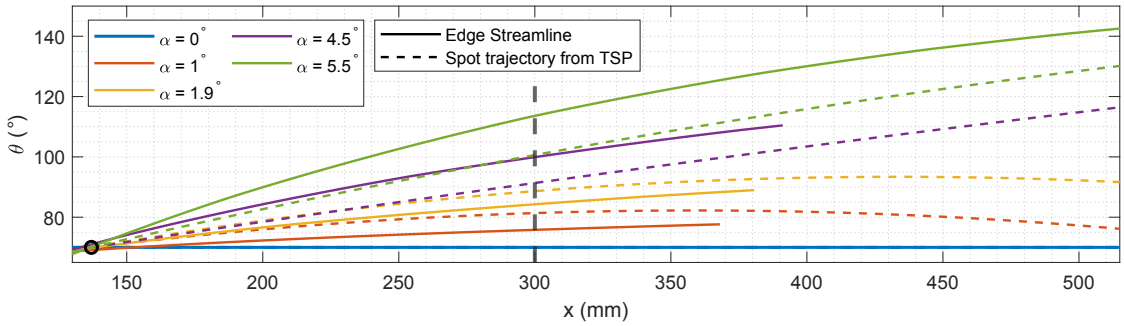

Fig. 15 Comparison of edge streamline vs extracted trajectory for different α

16(b). Since the development of turbulence is retarted by favorable pressure gradients, it is expected that the spreading rates of the turbulent spots in larger α cases would be smaller.

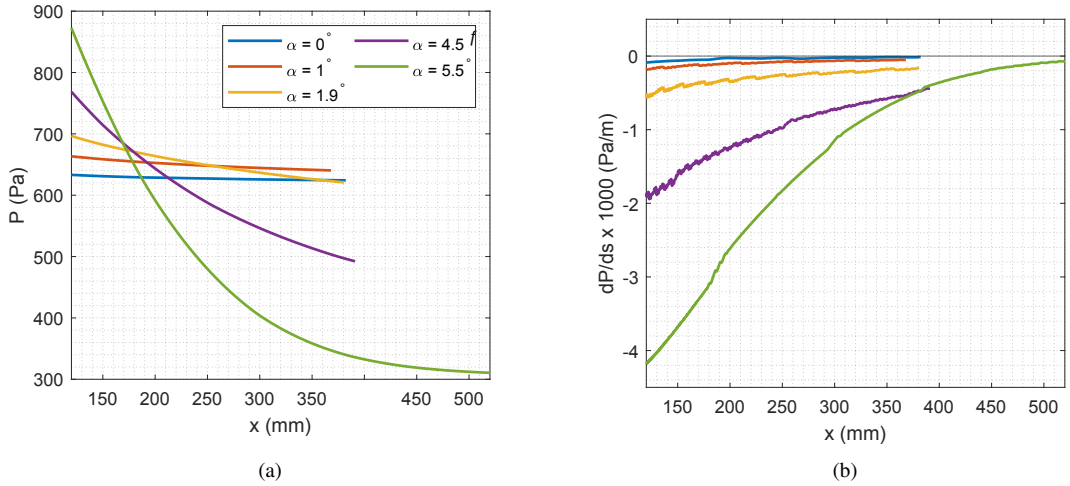

(a) (b)

Fig. 16 (a) Mean pressure along the edge streamline for different α obtained from computations, (b) Pressure gradient along the edge streamline.

A comparison of the slope of the trajectory of the spot centerline and its spanwise edges can be used to provide an estimate of the spot spreading rates. Unlike the zero angle of attack case, the spot trajectories for a pitched cone are curved as discussed above. As such the spreading rates vary continuously along the cone and can be computed for each x location. This is shown in Fig. 17(a) for all α for both the upper (lee side) and the lower (wind) side edges of the spot. The spreading rates appear symmetric about the centerline. For zero α, a constant value of 4.7° was observed. For small α, the spreading rates are observed to increase in the downstream direction. This could be atributed to the decrease in the -ve pressure gradient (see Fig. 16(b)) that would decrease the suppression of turbulence and increase the growth rates. Fig. 13 shows that this could also be related to the combining of the heat streak producing vortices with the turbulent spot. Due to the limited availability of the spot heating data near the downstream part of the cone, the errors in

the spot dimensions in that region can also increase the estimated spot spreading rates. So to make the comparisons more robust, an averaged spreading rate has been computed that represents an averaged value across the TSP field of view (x = 300-515 mm) for both the lower and upper edges of the spot. Fig. 17(b) shows a value of 5.2° and 5.4° which is comparable to the spreading rate observed at zero α. For larger α, the spreading rates are strongly diminished as expected by the strong favorabe pressure gradients in these cases (see Fig. 16(b)). This is demonstrated by the narrow region of diffuse turbulence in Fig. 14. An average value was computed by comparing the slopes and a value of 1.0° and 0.6° was obtained.

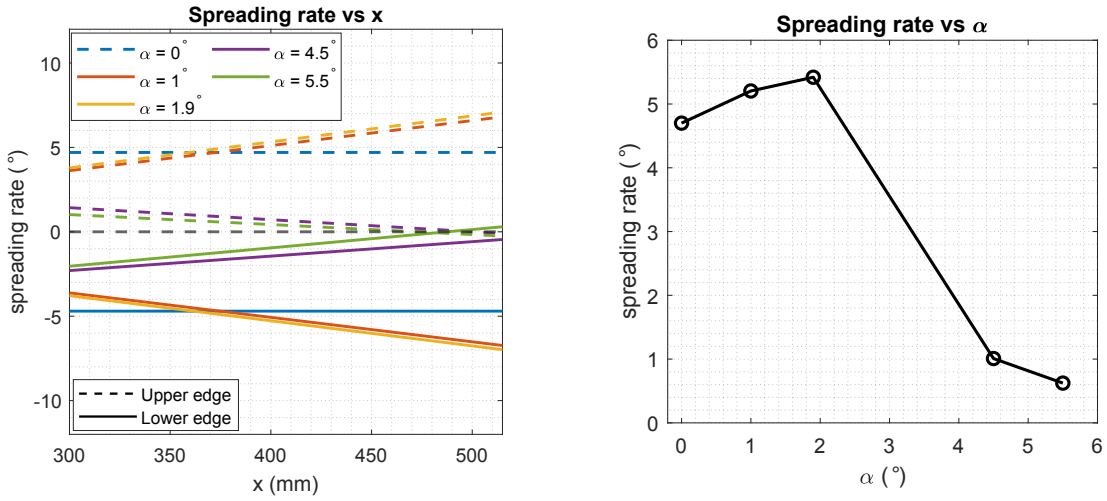

(a) (b)

Fig. 17 (a) Spreading rate for the lower and upper edge of the spot at all angles of attack, (b) Averaged spreading rate vs α

IV. Conclusions

An electric discharge perturber was used to inject disturbances in the boundary layer developing over a sharp cone at an angle of attack. The evolution of these disturbances was tracked using surface pressure and temperature sensors as well as optical diagnotics such as schlieren and TSP. The disturbances produced significant changes in the boundary layer characteristics as observed by increased intermittency in the pressure time series and spectra as well as sharp peaks at the forcing frequency in the schlieren visualizations. Use of a high forcing frequency resulted in a continous stream of turbulent spots that increased the heating on the cone as measured using the surface thermocouple data. This heating was exploited to extract the spot trajectory using TSP at different angles of attack. At α = 0°, a spreading rate of 4.7° was obtained on the cone. For the small α tested, the spreading rate was found to be comparable to the zero degree case, while it decreased strongly for large α cases. A pair of heating streaks generated by either discharge blockage induced or roughness induced vortices interacted with the developing spot. At small α, these vortices merged and diffused into the

turbulent spot while at larger α, these vortices remained laminar and coherent. This could be due to the favourable pressure gradient that suppressed turbulence and prevented the vortices from transitioning. For small α cases, the spot trajectory in the TSP field of view tracked the edge streamlines that pass through the perturber location. On the other hand, at larger α the spot trajectory diverged to the wind side of the edge streamlines. It is suggested that the favorable azimuthal pressure gradient that exists on the lee side of the streamline prohibits the growth of turbulence as seen in the delay of transition of the vortices inducing the heat streaks. As such the turbulence in the spot develops on the wind side of the streamline where the adverse pressure gradient enhances turbulence. This results in a spot that grows obliquely to the local edge streamline. Further work is needed to corroborate this finding; future work would include analysis of the surface sensor data and schlieren images to compare the characteristics of the streaks and the spots.

V. Acknowledgments

Melissa Soehnel helped with the data-acquisition and Seth Spitzer painted TSP on the model. Neal Bitter performed the US3D computations. Sandia National Laboratories is a multi-mission laboratory managed and operated by National Technology and Engineering Solutions of Sandia, LLC., a wholly owned subsidiary of Honeywell International, Inc., for the U.S. Department of Energy's National Nuclear Security Administration under contract DE-NA0003525.

References

[1] Schneider, S. P., "Hypersonic laminar–turbulent transition on circular cones and scramjet forebodies," *Progress in Aerospace Sciences*, Vol. 40, No. 1-2, 2004, pp. 1–50. doi:10.1016/j.paerosci.2003.11.001.

[2] Babinsky, H., and Harvey, J. K., *Shock Wave-Boundary-Layer Interactions*, 1st ed., Cambridge University Press, 2012. doi:10.1017/CBO9780511842757.

[3] Pandey, A., Casper, K. M., Spillers, R. W., Soehnel, M., and Spitzer, S., "Hypersonic Shock Wave-Boundary-Layer Interaction on the Control Surface of a Slender Cone," *AIAA SciTech 2020 Forum*, 2020, p. 0815. doi:10.2514/6.2020-0815.

[4] Fedorov, A., "Transition and Stability of High-Speed Boundary Layers," *Annual Review of Fluid Mechanics*, Vol. 43, No. 1, 2011, pp. 79–95. doi:10.1146/annurev-fluid-122109-160750.

[5] Zhong, X., and Wang, X., "Direct Numerical Simulation on the Receptivity, Instability, and Transition of Hypersonic Boundary Layers," *Annual Review of Fluid Mechanics*, Vol. 44, 2012, pp. 527–561.

[6] Sankaran, R., Sokolov, M., and Antonia, R. A., "Substructures in a turbulent spot," *Journal of Fluid Mechanics*, Vol. 197, No. 389-414, 1988. doi:10.1017/S0022112088003295.

[7] Johansson, A. V., Her, J.-Y., and Haritonidis, J. H., "On the generation of high-amplitude wall-pressure peaks in turbulent boundary layers and spots," *Journal of Fluid Mechanics*, Vol. 175, 1987, pp. 119–142. doi:10.1017/S0022112087000326.

[8] Wu, X., Moin, P., Wallace, J. M., Skarda, J., Lozano-Duran, A., and Hickey, J.-P., "Transitional–turbulent spots and turbulent–turbulent spots in boundary layers," *Proceedings of the National Academy of Sciences of the United States of America*, Vol. 114, No. 27, 2017, pp. E5292–E5299. doi:10.1073/pnas.1704671114.

[9] Emmons, H. W., "The Laminar-Turbulent Transition in a Boundary Layer-Part I," *Journal of Aeronautical Sciences*, Vol. 18, No. 7, 1951, p. 490. doi:10.2514/8.2010.

[10] Dhawan, S., and Narasimha, R., "Some properties of boundary layer flow during the transition from laminar to turbulent motion," *Journal of Fluid Mechanics*, Vol. 4, No. 3, 1958, pp. 418–436. doi:10.1017/S0022112058000094.

[11] Schubauer, G. B., and Klebanoff, P. S., "Contributions on the mechanics of boundary-layer transition," *NACA Technical Report*, Vol. 3489, 1955.

[12] Wygnanski, I. J., Sokolov, M., and Friedman, D., "On a turbulent 'spot' in a laminar boundary layer," *Journal of Fluid Mechanics*, Vol. 78, No. 4, 1976, pp. 785–819. doi:10.1017/S0022112076002747.

[13] Perry, A. E., Lim, T. T., and Teh, E. W., "A visual study of turbulent spots," *Journal of Fluid Mechanics*, Vol. 104, No. 3, 1981, pp. 387–405. doi:10.1017/S0022112081002966.

[14] Cantwell, B., Coles, D., and Dimotakis, P., "Structure and entrainment in the plane of symmetry of a turbulent spot," *Journal of Fluid Mechanics*, Vol. 87, No. 4, 1978, pp. 641–672. doi:10.1017/S0022112078001809.

[15] Nolan, K. P., and Zaki, T. A., "Conditional sampling of transitional boundary layers in pressure gradients," *Journal of Fluid Mechanics*, Vol. 728, 2013, pp. 306–339. doi:10.1017/jfm.2013.287.

[16] Katz, Y., Seifert, A., and Wygnanski, I., "On the evolution of the turbulent spot in a laminar boundary layer with a favourable pressure gradient," *Journal of Fluid Mechanics*, Vol. 221, 1990, pp. 1–22. doi:10.1017/S0022112090003469.

[17] Fischer, M. C., "Spreading of a turbulent disturbance," *AIAA Journal*, Vol. 10, No. 7, 1972, pp. 957–959. doi:10.2514/3.50265.

[18] Krishnan, L., and Sandham, N. D., "Effect of Mach number on the structure of turbulent spots," *Journal of Fluid Mechanics*, Vol. 566, 2006, pp. 225–234. doi:10.1017/S0022112006002412.

[19] Casper, K. M., Beresh, S. J., and Schneider, S. P., "Pressure fluctuations beneath instability wavepackets and turbulent spots in a hypersonic boundary layer," *Journal of Fluid Mechanics*, Vol. 756, 2014, pp. 1058–1091. doi:10.1017/jfm.2014.475.

[20] Gordeyev, S., and Juliano, T. J., "Optical measurements of transitional events in a Mach-6 boundary layer," *AIAA Journal*, Vol. 55, 2017, pp. 3629–3639. doi:10.2514/1.J055759.

[21] Ozawa, H., "Experimental study of unsteady aerothermodynamic phenomena on shock-tube wall using fast-response temperature-sensitive paints," *Physics of Fluids*, Vol. 28, No. 4, 2016, p. 046103. doi:10.1063/1.4947040.

[22] Mee, D. J., "Boundary-layer transition measurements in hypervelocity flows in a shock tunnel," *AIAA Journal*, Vol. 40, No. 8, 2002, pp. 1542–1548. doi:10.2514/2.1851.

[23] Fiala, A., Hillier, R., Mallinson, S. G., and Wijesinghe, H. S., "Heat transfer measurement of turbulent spots in a hypersonic blunt-body boundary layer," *Journal of Fluid Mechanics*, Vol. 555, 2006, pp. 81–111. doi:10.1017/S0022112006009396.

[24] Jewell, J. S., Leyva, I. A., and Shepherd, J. E., "Turbulent spots in hypervelocity flow," *Experiments in Fluids*, Vol. 58, No. 32, 2017. doi:10.1007/s00348-017-2317-y.

[25] Casper, K. M., Beresh, S. J., Henfling, J. F., Spillers, R. W., Hunter, P., and Spitzer, S., "Hypersonic fluid-structure interactions due to intermittent turbulent spots on a slender cone," *AIAA Journal*, Vol. 57, No. 2, 2019, pp. 749–759. doi:10.2514/1.J057374.

[26] Robbins, B. A., Casper, K. M., Coffin, P., Mesh, M., and Field Jr., R. V., "Quantifying the structural response of a slender cone to turbulent spots at mach 6," *AIAA Scitech 2019 Forum*, American Institute of Aeronautics and Astronautics Inc, AIAA, San Diego, CA, 2019. doi:10.2514/6.2019-1631.

[27] Liu, T., and Sullivan, J. P., *Pressure and Temperature Sensitive Paints*, Springer-Verlag Berlin Heidelberg, 2005. doi: 10.1007/b137841.

[28] Gronvall, J. E., Johnson, H. B., and Candler, G. V., "Hypersonic three-dimensional boundary layer transition on a cone at angle of attack," *42nd AIAA Fluid Dynamics Conference and Exhibit 2012*, American Institute of Aeronautics and Astronautics Inc., 2012. doi:10.2514/6.2012-2822.

[29] Casper, K. M., Beresh, S. J., Henfling, J. F., Spillers, R. W., Pruett, B. O., and Schneider, S. P., "Hypersonic wind-tunnel measurements of boundary-layer transition on a slender cone," *AIAA Journal*, Vol. 54, No. 4, 2016, pp. 1250–1263. doi:10.2514/1.J054033.